mater.scichina.com link.springer.com Published online 3 March 2023 | https://doi.org/10.1007/s40843-022-2366-4

Three-dimensional weak localization and negative magnetoresistance in high-quality PtP_2 crystals

Qiuzhen Cheng[1,2†], Guoyu Xian[2,3†], Yin Huang[2,3], Hui Guo[2,3,4], Lulu Pan[2], Houbo Zhou[2,3], Jing Wang[2,3], Senhao Lv[2], Chengmin Shen[2,3,4], Xiao Lin[3], Hailong Chen[2,3], Yongfeng Li[1*], Haitao Yang[2,3,4*] and Hong-Jun Gao[2,3,4]

ABSTRACT **Pentagonal-ring-structured PtP_2 bulk crystals and the two-dimensional (2D) PtP_2 with rich theoretical physical and chemical properties have attracted considerable attention for the applications in high-performance electronic and optoelectronic devices. Here, high-quality PtP_2 single crystals have been successfully prepared by using a tin flux method with the optimal molar ratios of Pt and P. 3D weak localization effect and negative magnetoresistance (NMR) are observed in the high-quality PtP_2 single crystals for the first time. Crystalline structure, magnetization, and optical spectral characterizations have demonstrated that the defects in PtP_2 crystals can suppress the NMR effect and magnetic ordered states. These findings open up a way to synthesize the bulk and low-dimensional noble-metal-based phosphides of high quality and provide new platforms for studying the different correlated electronic states.**

Keywords: PtP_2, single crystal, pentagonal-ring-structure, 3D weak localization, negative magnetoresistance

INTRODUCTION

Transition metal phosphides (TMPs) are an important class of functional materials because of their unique structural features and outstanding properties such as hardness, electronic and chemical stability [1–3]. TMPs are well known as high-performance battery materials and catalysts for various hydrotreatment processes, such as hydrogen desulphurization, hydrogen denitrogenation, and electrocatalysis [4,5]. In addition, TMPs, such as LaP_2, ScP_4, and YP_2, have been reported to exhibit superconductivity under pressure in experiments and theoretical calculations [6,7]. GeP_3 monolayer with tunable bandgaps and strong interlayer quantum confinement effects, InP_3 and SnP_3 monolayers with high carrier mobilities and strain-controlled bandgaps have been predicted in theory [8,9]. However, the developments and applications of TMPs have been greatly hindered because the synthesis of TMP crystals and low-dimensional materials requires high temperature or high pressure with flammable elemental phosphorus as the phosphorus source, making the experiments difficult and dangerous to be conducted.

Recently, platinum-based TMPs have attracted considerable attention owing to their rich physical properties, mainly from the strong spin-orbit coupling of the platinum 5d electrons. A prominent example is the newly reported family of APt_3P (A = Ca, Sr, Ce, and La) with a tetragonal structure. For instance, $CaPt_3P$ and $SrPt_3P$ exhibit conventional superconductivity, $CePt_3P$ as a moderately correlated antiferromagnetic Kondo lattice compound shows a coexistence of antiferromagnetic ordering, Kondo effect and crystalline electric field effect [10–12], while $LaPt_3P$ is a d-wave singlet superconducting ground state with topologically protected Majorana Fermi-arcs and a Majorana flat band. A Pt_2P layer in $LaPt_3P$ has an important role resembling the "mothered" FeAs layer in the iron-based superconductors [13]. Moreover, the pentagon-ring-structured PtP_2 monolayer is theoretically predicted as a direct band gap semiconductor with surprisingly high carrier mobility of 14.4×10^4 $cm^2 V^{-1} s^{-1}$ and strong optical absorption, which has potential applications in high-speed electronic devices and optoelectronics [14]. Unlike previously theoretically reported single-layer pentagonal-structured materials such as $PdSe_2$, AgN_3, SiC_2, CN_2, and B_2C [15–19] with a buckled Cairo tessellation, PtP_2 monolayer exhibits the ideal Cairo tessellation with completely coplanar Pt and P atoms [20]. Importantly, this hidden Cairo tessellation in PtP_2 bulk phase has been examined with density functional theory calculations, which provide the great possibility of obtaining a single-layer PtP_2 with the Cairo tessellation from the bulk by a chemical exfoliation technique for chemically bonded bulk phases, like extracting a single layer (MXene) from transition metal carbides or nitrides [21,22]. Considering the extreme difficulty in the direct synthesis of single-layer PtP_2, it is necessary to develop a facile method to prepare the high-quality PtP_2 single crystal, modulate its physical properties and achieve single-layer PtP_2 by the chemical exfoliation.

In this study, PtP_2 single crystals are successfully prepared with the tin flux method. By changing the molar ratios of Pt and P, PtP_2 single crystals with a high crystal quality can be achieved,

[1] State Key Laboratory of Heavy Oil Processing, China University of Petroleum, Beijing 102249, China
[2] Beijing National Center for Condensed Matter Physics and Institute of Physics, Chinese Academy of Sciences, Beijing 100190, China
[3] School of Physical Sciences, University of Chinese Academy of Sciences, Beijing 100190, China
[4] Songshan Lake Materials Laboratory, Dongguan 523808, China
† These authors contributed equally to this work.
* Corresponding authors (emails: yfli@cup.edu.cn (Li Y); htyang@iphy.ac.cn (Yang H))

which is determined by the full width at half maximum (FWHM) of rocking curves. By electrical transport measurements, we observed a three-dimensional (3D) weak localization effect and negative magnetoresistance (NMR) in the high-quality PtP_2 crystals. Furthermore, we found that the defects in the PtP_2 single crystals can suppress the NMR effect and magnetic ordered states, which is confirmed by the crystalline structure, magnetization, and optical spectral characterizations. Our work opens up a way to synthesize high-quality PtP_2 single crystals with rich electronic and optical properties and provides a great potential for application in diverse electronics and optoelectronics.

EXPERIMENTAL SECTION

PtP_2 single crystals were obtained by using the Sn-flux method [23]. High-purity platinum (99.99%, powder), red phosphorus (99.999%, lump), and tin (99.999%, shot) were loaded in a graphite crucible with molar ratios of 1:4:30 (named as S1) and 1:2.5:30 (named as S2), and then sealed in a quartz ampule. The mixture was heated to 1423 K at a rate of 10 K h^{-1} and kept there for three days. Then the crucible was slowly cooled down to 823 K at a rate of 5 K h^{-1} followed by cooling down to room temperature naturally. Finally, the tin flux was removed by 2 N solution of hydrochloric acid.

Temperature-dependent X-ray diffraction (XRD) measurements were carried out on a Rigaku SmartLab X-ray diffractometer with Cu-Kα radiation and the cooling sample stage. Rocking curves were obtained from Bruker D8 Venture with Cu-Kα radiation. Scanning electron microscopy (SEM) images and X-ray energy dispersive spectroscopy (EDS) analyses were carried out on Hitachi SU5000 with Bruker Quantax XFlash 6160. High-resolution transmission electron microscopy (HRTEM) images and selected-area electron diffraction (SAED) images were collected on a JEOL JEM-2100Plus. X-ray photoelectron spectroscopy (XPS) data were collected using a VG ESCALAB-5. Raman spectra and photoluminescence (PL) spectroscopy were assembled on a WITec ALPHA300R.

Electrical transport properties and specific heat capacity (C_p) measurements were carried out on a Quantum Design physical property measurement system (PPMS). A standard Hall bar with indium strip as electrodes was fabricated to measure the electrical transport properties. The magnetization measurement was conducted on a Quantum Design magnetic property measurement system (MPMS), where the applied magnetic field was perpendicular to the (201) plane. Femtosecond time-resolved mid-infrared (IR) absorption spectroscopy measurements were carried out by using the output pulses from a femtosecond amplifier laser system (Spitfire Ace, Spectra-Physics) with the pulse duration of ~35 fs. The wavelengths of pump and probe pulses are 400 and 5000 nm, respectively. And the excitation-induced transmission change of the probe light was collected by a spectrograph (iHR 320, HORIBA Jobin Yvon).

RESULTS AND DISCUSSION

Bulk PtP_2 has a cubic pyrite structure with the space group of *Pa*3 and the lattice constant a = 5.69 Å. The side view of the lattice structure is shown in Fig. 1a. The primitive unit cell contains four Pt and eight P atoms. Pt atoms form a face-centered cubic structure and P atoms surrounded Pt form an inclined octahedron structure (Fig. S1). Fig. 1b shows the top view and side view of the PtP_2 monolayer cut from the *ab* plane. From the top view, each Pt atom adopts a planar tetracoordinate with four P atoms, forming a beautiful pentagonal ring network known as the Cairo pentagonal tiling geometry.

During the preparation of high-quality PtP_2 single crystals, we find the starting molar ratio of Pt and P is a crucial factor impacting the crystalline quality. We compared the structures and physical properties of two samples fabricated with different

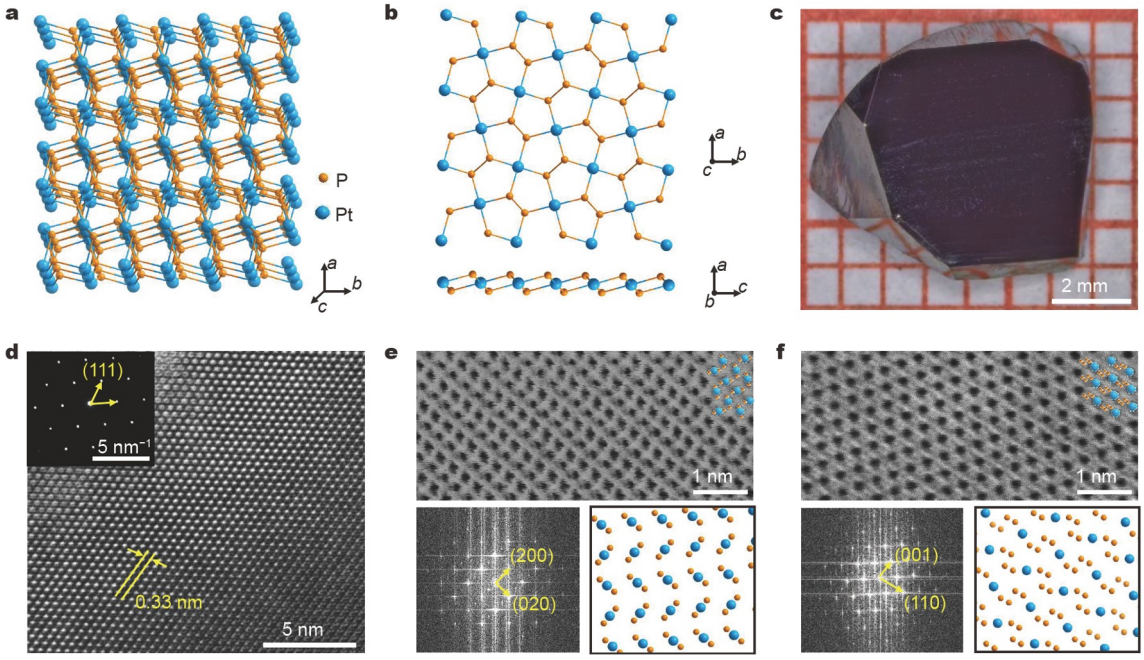

Figure 1 (a) An atomic structure model of PtP_2 bulk crystals. (b) The top view and side view of the atomic model for PtP_2 monolayer on the *ab* plane. (c) The photo of a typical PtP_2 crystal. (d) HRTEM image and SAED pattern of the PtP_2 crystal, showing the (111) plane. (e, f) STEM bright field images of PtP_2 at different planes. The bottom panels show the corresponding fast Fourier transform images (left) and atomic structure models (right), respectively.

starting molar ratios, Pt:P (1:4) and Pt:P (1:2.5), named S1 and S2, respectively. Fig. 1c displays a typical photograph of the as-grown PtP_2 single crystal (S1) with sharply defined edges and the average crystal size of 7 mm × 7 mm. The HRTEM image in Fig. 1d shows a lattice spacing of 0.33 nm in three directions with the angle of 60° corresponding to the (111) plane of PtP_2 ($d_{(111)}$ = 0.328 nm, PDF card No. 5910111), which is consistent with the SAED image in the inset of Fig. 1d. Atomic-resolved scanning TEM (STEM) bright-field images of S1 (Fig. 1e and f viewed along the [002] and [$\bar{1}$10] projection, respectively) show the perfect atomic arrangements of S1 without atomic defects and impurity atoms, which is consistent with the atomic structure model of PtP_2. The powder XRD was conducted for the grinded S1 (Fig. S2a). All peaks are consistent with the standard pattern of PtP_2 (PDF card No. 5910111). Moreover, the temperature-dependent XRD patterns of S1 was collected on a fresh polished (210) crystalline plane (Fig. S2b). Two strong reflection peaks at 2θ = 35.5° and 74.5° are corresponding to (210) and (420) planes. The peak location of the (420) plane has no obvious shift (right part of Fig. S2a), which demonstrates no structure phase transitions occur in the temperature range from 300 to 5 K. The chemical composition of S1 was determined by EDS. Fig. S3 shows the SEM and EDS mapping results. The surface of S1 is smooth and flat. The distributions of Pt and P elements are uniform. And the chemical composition of Pt:P is close to 1:2 (inset table of Fig. S3d). XPS was employed to obtain the atomic valence states of Pt and P. As shown in Fig. S4, the XPS signal of Pt shows two strong peaks for $4f_{7/2}$ at 73.9 eV and $4f_{5/2}$ at 77.3 eV corresponding to the Pt–P bond in PtP_2. Similarly, the P 2p signal shows two peaks at 130.0 and 130.9 eV corresponding to $2p_{3/2}$ and $2p_{1/2}$ of the P–Pt bond in PtP_2. It should be noted that the results of EDS, TEM, and XPS for S2 are identical to those of S1.

In order to investigate the electronic transport properties, the temperature-dependent longitudinal resistivities of S1 and S2 were acquired in the temperature range from 300 to 4 K. As shown in Fig. 2a, the resistivities (ρ_1 and ρ_2) of S1 and S2 increase with decreasing temperature. Both samples exhibit typical semiconducting characteristics. By comparing S1 and S2, there is no significant difference between the resistivities of the two samples at room temperature (ρ_1(300 K) = 2.0 × 10^{-4} Ω m, ρ_2(300 K) = 1.6 × 10^{-4} Ω m). However, ρ_1 at 4 K is four orders of magnitude larger than ρ_2 at 4 K. For S1, ρ_1 increases sharply when the temperature is below 50 K with a transition point around 25 K. But for S2, ρ_2 increases significantly below the temperature of 12 K. Fig. 2b, c display the Hall coefficients (R_H) of S1 and S2 at different temperatures. The Hall coefficients are extracted from the corresponding ρ_{xy}-H (magnetic field intensity) curves (the insets of Fig. 2b, c), which show linear dependence with positive slopes. The Hall coefficients of the two samples are positive in the range from 300 to 4 K, indicating that the PtP_2 single crystal is an n-type semiconductor with electrons as the dominant carriers. As the temperature decreases, the R_H of S1 increases slightly in the temperature range from 300 to 50 K and then a small decrease happens between 50 and 25 K, while the R_H increases sharply when the temperature drops from 25 to 4 K. Unlike S1, the R_H of S2 increases slowly in the whole

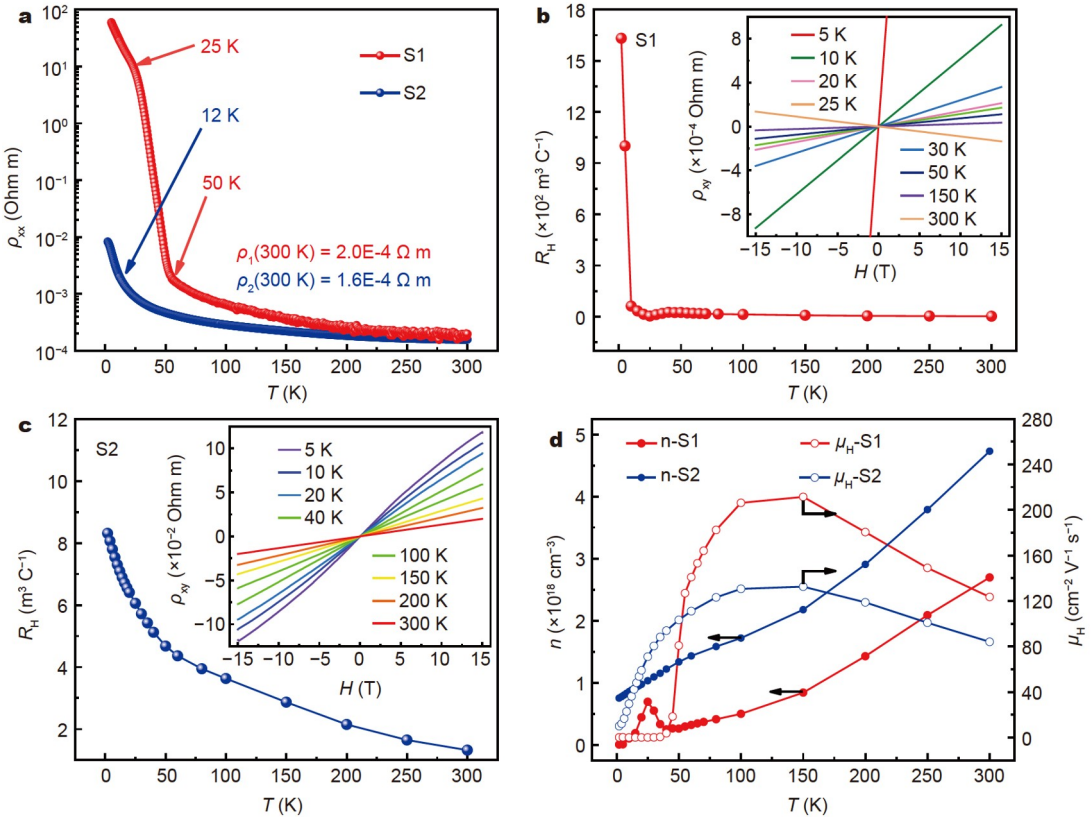

Figure 2 (a) Temperature-dependent longitudinal resistivities of S1 and S2 in the temperature range from 4 to 300 K. (b, c) The temperature dependence of Hall coefficients R_H of S1 and S2. The insets: R_H extracted from ρ_{xy}-H curves at various temperatures. (d) The carrier concentration n and the Hall mobility μ at different temperatures of S1 and S2.

temperature range from 300 to 4 K. And the R_H of S2 is two orders of magnitude smaller than that of S1 at 4 K. Similarly, the carrier concentration and the Hall mobility at different temperatures can be extracted from the corresponding ρ_{xy}-H curves of S1 and S2. As shown in Fig. 2d, the carrier concentration of both S1 and S2 can reach a high-level of 10^{18} cm^{-3} at room temperature, which is in the same order of magnitude as GaN [24]. With the temperature decreasing, the carrier concentration of S1 and S2 decreases linearly, which is a typical characteristic of semiconductor. The carrier concentration of S1 is always smaller than that of S2 in the whole range from 300 to 4 K. It is interesting that an anomaly is observed at 25 K in S1. The Hall mobilities of S1 and S2 show a nonlinear change from 4 to 300 K and have the maximum values of 211 and 130 cm^{-2} V^{-1} s^{-1} at 150 K, respectively.

To further investigate the electronic transport performance of the PtP_2 single crystals, magneto-transport measurements of S1 and S2 were carried out under the magnetic field perpendicular to the (210) plane. The MR, defined as MR = $[(R(H) - R(0)) / R(0)] \times 100\%$, was measured below 50 K and in the magnetic field range from −15 to 15 T. Overall, both the MRs of S1 and S2 exhibit a parabolic relationship to the magnetic field. The NMR effects appear near zero magnetic field below 50 K in S1, whereas it is below 14 K in S2, as shown in Fig. 3. The MR experimental results and the corresponding fitting of S1 are shown in Fig. 3a–f. The largest MR of S1 under a magnetic field of 15 T is 23.3% at 50 K (Fig. 3a). Fig. 3b–d exhibit the MR-H curves in the magnetic field range from −4 to 4 T below 50 K. The NMR effects show a non-monotonic change with increasing temperature, i.e., NMR value decreases from 5 to 20 K, (Fig. 3b) while increases from 20 to 35 K (Fig. 3c), and then decreases from 35 to 45 K (Fig. 3d).

Generally speaking, the NMR effects originate from weak localization, Kondo effect or chirality anomaly. Firstly, the NMR effect caused by chirality anomaly generally exists in the magnetic semimetal with chiral lattices and is dependent on the angle between the magnetic field and current. PtP_2 is a semiconductor without chiral lattices and the angle-dependent MR is not observed in our MR results of S1, which indicates the chirality anomaly is absence in S1. Secondly, the Kondo effect can be excluded because the NMR cannot be fitted by a quadratic relationship (MR (%) = $aH^2 + b$) [25].

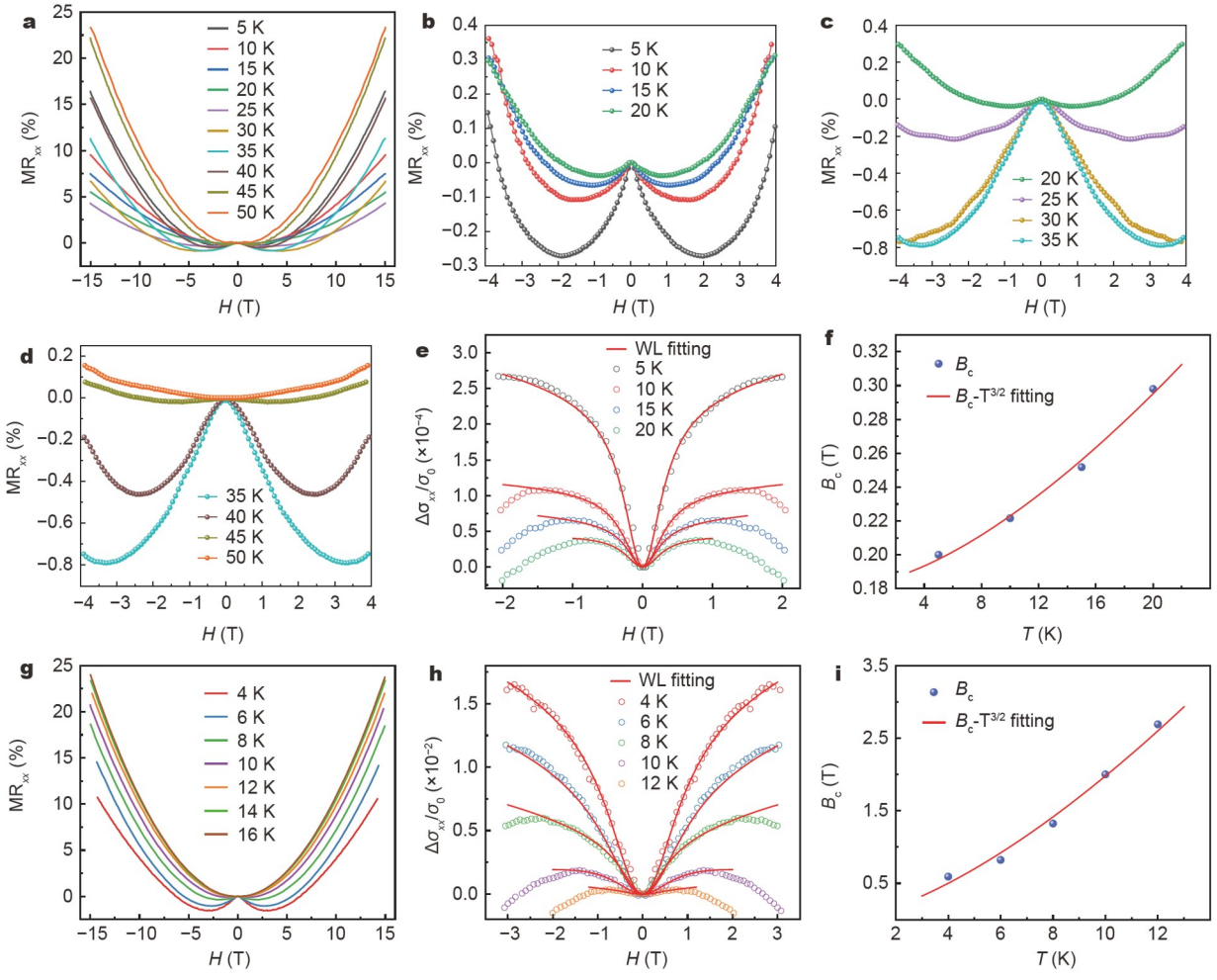

Figure 3 (a) Magnetoresistance of S1 at 5–50 K and 0–15 T. (b) Weak localization effect of S1 under low magnetic fields of 5–20 K. (c) Electron-electron interaction of S1 under low magnetic fields of 20–35 K. (d) Negative MR of S1 under low magnetic fields of 35–50 K. (e) $\Delta\sigma_{xx}/\sigma_0$ of S1 as a function of low magnetic field at 5–20 K (WL stands for weak localization). The circles represent experimental results. The solid lines are fitting results. (f) B_c extracted from weak localization fitting results of S1. The solid line is B_c *vs.* $T^{3/2}$ fitting results. (g) Magnetoresistance of S2 at 4–16 K and 0–15 T. (h) $\Delta\sigma_{xx}/\sigma_0$ of S2 as a function of low magnetic field at 5–20 K. The circles represent experimental results. The solid lines are fitting results. (i) Critical field B_c extracted from weak localization fitting results of S2. The solid line is B_c *vs.* $T^{3/2}$ fitting results.

The 3D weak localization formula [26] is used to fit the relationship between the conductivity and the magnetic field at 5–20 K.

$$\frac{\Delta\sigma}{\sigma(0)} = \frac{1}{\sigma(0)}\left(C_1 \frac{B^2\sqrt{B}}{B_c^2+B^2} + C_2 \frac{B_c^2 B^2}{B_c^2+B^2}\right),$$

where the fitting parameters C_1 and C_2 are constants, and B_c is the critical magnetic field. $\Delta\sigma = \sigma(B) - \sigma(0)$, $\sigma(B)$ and $\sigma(0)$ are the conductivities with and without the magnetic field, respectively. C_1 and C_2 are positive for weak localization and negative for weak anti-localization. B_c is in direct proportion to T^p ($p > 0$). When $p = 3/2$ and $p = 3$, the decoherence mechanism is ascribed to the electron-electron interaction and the electron-phonon interaction, respectively. Based on the above formula, the experimental data at 5–20 K in Fig. 3e can be well fitted, indicating the NMR is caused by 3D weak localization. Furthermore, after B_c is extracted from the fitting data in Fig. 3e, the relationship between B_c and T is well fitted by $T^{3/2}$ (Fig. 3f), which indicates that the 3D weak localization originates from the electron-electron interaction. The NMR at 20–35 K becomes strong again with increasing temperature, which may be caused by the electron-electron interaction [27]. At 35–45 K, the NMR decreases gradually with increasing temperature, which is mainly caused by the supersession of the electron-electron interaction by the electron-phonon scattering.

The MR-H curves of S2 in the temperature range from 4 to 14 K and under the magnetic fields from −15 to 15 T were measured, as shown in Fig. 3g. In the S2 case, the NMR also appears below 12 K and 3 T. And the NMR decreases as the temperature increases and converts to the normal positive MR behavior above 14 K. Similarly, in the range of 4–14 K, the NMR of S2 is caused by 3D weak localization related to the electron-electron interaction. However, the critical temperature of 3D weak localization of S2 decreases to 14 K compared with that of S1 (50 K). Besides, at the same temperature, the B_c of S1 is much smaller than that of S2. As we know, the weak localization comes from the electron coherent backscatter caused by impurities or defects. The magnetic field is used to destroy the phase coherence. The more defects or impurities, the greater magnetic field is required to break the phase coherence. Therefore, the larger critical field of S2 suggests that there are more defects or impurities in S2 than S1.

In order to further confirm the strong correlation between the physical properties of PtP_2 crystals with their crystal qualities, a series of systematical characterizations were performed. The XRD ω scan rocking curves for the (420) plane of S1 and S2 are shown in Fig. 4a. The FWHMs of the diffraction peaks of S1 and S2 are 0.24° and 0.45°, respectively, which indicates that S1 has a better crystal quality. The Raman spectra of PtP_2 for S1 shows four feature peaks: the stretching mode (A_g) of the P–P bond at 486 cm^{-1}, the rocking mode (E_g) of the P–Pt bond at 364 cm^{-1}, and other two weak peaks related to the coupling of the stretching mode and the rocking mode at 511 cm^{-1} (F_{g1}) and 378 cm^{-1} (F_{g2}) [28]. The Raman spectra of S2 have been fitted to four feature peaks. Obviously, all of the four peaks of S2 are wider than those of S1 along with a red-shift ($\Delta \approx 7$ cm^{-1}), which indicates the change of phonon spectral induced by the defects in S2.

The PL spectroscopy in Fig. 4c can be fitted to a strong peak (P1), a weak peak (P2), and a large bulge (P3). The strong peak located at 1.61 eV corresponds to the band gap of PtP_2, which is consistent with 1.60 eV obtained by the ultraviolet-visible-near

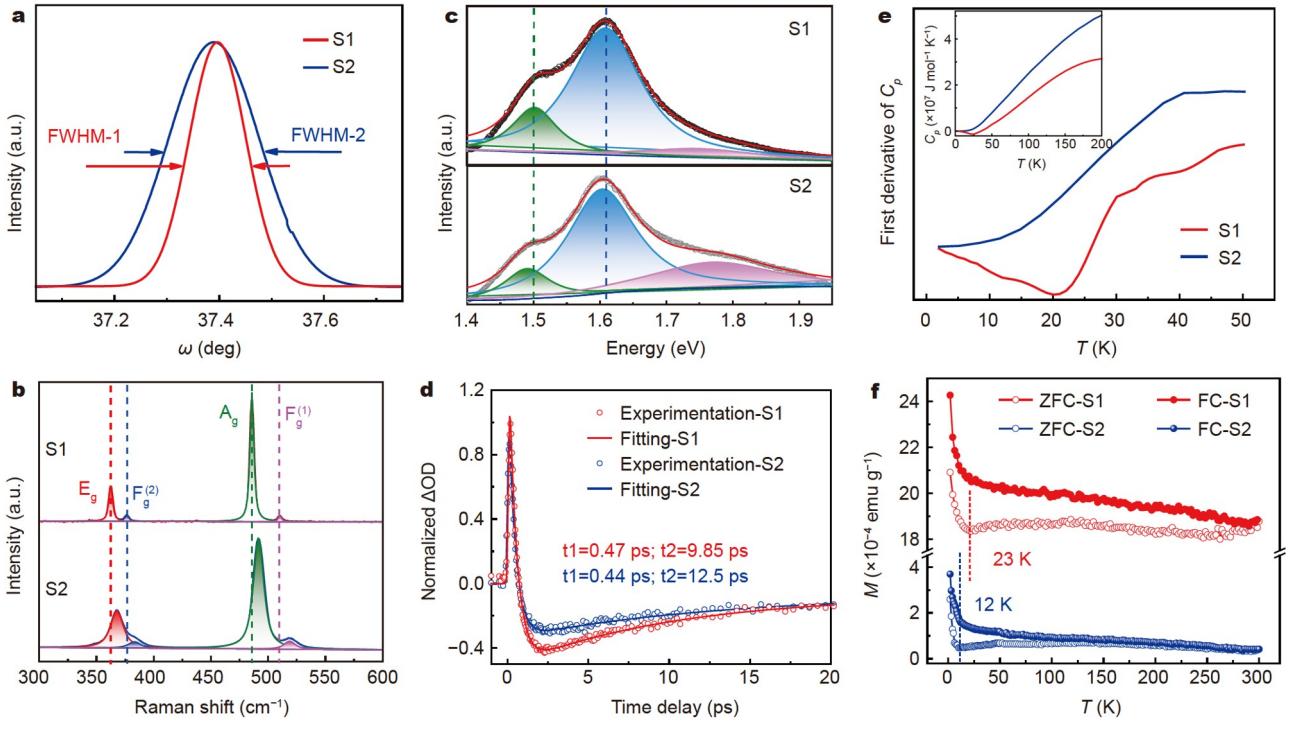

Figure 4 (a) Rocking curves of (420) plane for S1 and S2. (b) Raman spectra of S1 and S2. (c) The PL spectroscopy of S1 and S2 excited by 400 nm at room temperature. (d) The normalized transient absorption spectra of S1 and S2 in the MIR region measured as a function of time delay after excitation at 400 nm with 100 μJ cm^{-2} pump fluence. (e) The first derivative of heat capacity to temperature. The inset shows the heat capacity of S1 and S2 at 2–200 K. (f) Magnetization variation as a function of temperature for S1 and S2 under FC in 1000 Oe and ZFC conditions.

IR (UV-Vis-NIR) absorption spectra (Fig. S5). The weak peak at about 1.50 eV is the PL peak of PtP_2. The large bulge around 1.78 eV is caused by impurities or defects. Comparing the PL spectra of S1 and S2, it can be seen that the band gap of S2 is slightly smaller than that of S1 ($\Delta E \approx 0.01$ eV) and the bulge of S2 is much stronger than that of S1. The results also demonstrate that more defects exist in S2. The defects are possibly the P atomic vacancies since P atoms are easier to separate from the crystalline lattice than Pt atoms in the high-temperature growth environment. The vacancies of P atoms can result in a narrow bandgap of PtP_2 and make Pt ions to act as a charge donor, which can both provide more carriers to enhance electrical conductivity [29,30].

In the normalized transient absorption spectra in the mid-IR region (Fig. 4d), both dynamic curves of S1 and S2 exhibit a bi-exponential decay feature with two time constants of 0.47/9.85 ps and 0.44/12.5 ps, respectively. The excitation-induced positive signature in the mid-IR region is due to the free carrier absorption in the conduction band, so the fast decay corresponds to the relaxation of photoexcited free carriers. After the rapid relaxation, the slower decay process involves recombination and trapping of electrons and holes at the band edge. Photoexcited carriers trapped by defects were reported to induce the signature change from positive to negative in the mid-IR region [31], and the recovery process is closely related to the defect density. Therefore, the longer relaxation time of S2 (12.5 ps) than S1 (9.85 ps) also indicates larger defect density in S2.

In order to further reveal the origin of the transition point at 25 and 50 K, the C_p and temperature-dependent magnetization were measured. The decrease of C_p as the temperature decreases is in consistent with the trend of the Einstein model. There is no peak in the C_p curves in the temperature range from 2 to 200 K (inset of Fig. 4e), which indicates that PtP_2 has no first-order phase transition within the experimental temperature range and is consistent with the results of variable-temperature XRD. However, there is a weak drop on the C_p curve of S1 at about 25 K. To study the changing trend of C_p at low temperatures in detail, the first derivative of C_p at 2–50 K (Fig. 4e) shows that S1 has a drop peak around 20 K, while S2 has no obvious transition. So, there is a second-order phase transition for S1 around 20 K.

From the M-T curves of S1 and S2 (Fig. 4d), it can be found that the magnetization of S1 is stronger than that of S2, which indicates that there is a strong magnetic coupling in S1 due to its perfect crystallinity. In addition, the change trends of the field-cooled (FC) and zero-FC (ZFC) curves with the temperature are similar for S1 and S2. When the temperature drops to 23 K, the ZFC curve of S1 increases sharply. But the ZFC curve of S2 increases sharply until the temperature drops to 12 K. According to the absolute value of magnetism, the magnetic phase transitions may occur from disordered paramagnetic states to weak ordered magnetic states. Therefore, the electrical transport transition points may be caused by magnetic phase transitions of S1 and S2 at 23 and 12 K, respectively.

CONCLUSIONS

In summary, we have successfully prepared semiconducting PtP_2 crystals and systematically studied the crystalline structures and transport properties. The NMR and 3D weak localization were observed in PtP_2 single crystals for the first time. And a transition from the weak localization effect to the electron-electron interaction was also discovered, which may be caused by the transition of magnetic ordered states. In addition, the defects in PtP_2 crystals strongly affect the NMR and magnetic ordered states. Our work provides a promising platform to study various correlated electronic states in high-quality PtP_2 single crystals and is of great significance to explore the pentagonal-ring-structured PtP_2 monolayers.

Received 12 October 2022; accepted 19 December 2022; published online 3 March 2023

1 Lv YY, Xu J, Han S, *et al.* High-harmonic generation in Weyl semimetal β-WP_2 crystals. Nat Commun, 2021, 12: 6437
2 Qi L, Li A, Wang M, *et al.* Stable and efficient oxygen evolution from seawater enabled by graphene-supported sub-nanometer arrays of transition metal phosphides. Adv Mater Inter, 2022, 9: 2101720
3 Cao F, Zheng S, Liang J, *et al.* Growth of 2D MoP single crystals on liquid metals by chemical vapor deposition. Sci China Mater, 2021, 64: 1182–1188
4 Zhao Z, Zhu Z, Bao X, *et al.* Facile construction of metal phosphides (MP, M = Co, Ni, Fe, and Cu) wrapped in three-dimensional N,P-codoped carbon skeleton toward highly efficient hydrogen evolution catalysis and lithium-ion storage. ACS Appl Mater Interfaces, 2021, 13: 9820–9829
5 Zhou Q, Liao L, Bian Q, *et al.* Engineering in-plane nickel phosphide heterointerfaces with interfacial sp H-P hybridization for highly efficient and durable hydrogen evolution at 2 A cm^{-2}. Small, 2022, 18: 2105642
6 Li X, Zhang X, Yang Z, *et al.* Pressure-stabilized graphene-like P layer in superconducting LaP_2. Phys Chem Chem Phys, 2022, 24: 6469–6475
7 Zhao K, Yu H, Yang Q, *et al.* Emerging yttrium phosphides with tetrahedron phosphorus and superconductivity under high pressures. Chem Eur J, 2021, 27: 17420–17427
8 Miao N, Xu B, Bristowe NC, *et al.* Tunable magnetism and extraordinary sunlight absorbance in indium triphosphide monolayer. J Am Chem Soc, 2017, 139: 11125–11131
9 Zhu XL, Liu PF, Zhang J, *et al.* Monolayer SnP_3: An excellent p-type thermoelectric material. Nanoscale, 2019, 11: 19923–19932
10 Shi L, Yang P, Wang T, *et al.* Pressure effect in the antiperovskite phosphide superconductor $Sr(Pt_{0.9}Pd_{0.1})_3P$. Phys Rev B, 2022, 105: 214529
11 Aperis A, Morooka EV, Oppeneer PM. Influence of electron-phonon coupling strength on signatures of even and odd-frequency superconductivity. Ann Phys, 2020, 417: 168095
12 Makhaneva AY, Zakharova EY, Nesterenko SN, *et al.* Metal-rich phosphides obtained from the lead flux: Synthesis, crystal, and electronic structure of $Sr_5Pt_{12}P_9$ and $BaPt_3P_2$. Inorg Chem, 2022, 61: 9173–9183
13 Biswas PK, Ghosh SK, Zhao JZ, *et al.* Chiral singlet superconductivity in the weakly correlated metal $LaPt_3P$. Nat Commun, 2021, 12: 2504
14 Qian S, Sheng X, Xu X, *et al.* Penta-MX_2 (M = Ni, Pd and Pt; X = P and As) monolayers: Direct band-gap semiconductors with high carrier mobility. J Mater Chem C, 2019, 7: 3569–3575
15 Zhao Y, Yu P, Zhang G, *et al.* Low-symmetry $PdSe_2$ for high performance thermoelectric applications. Adv Funct Mater, 2020, 30: 2004896
16 Lin J, Wang F, Rui Q, *et al.* A novel square planar N_4^{2-} ring with aromaticity in BeN_4. Matter Radiat at Extremes, 2022, 7: 038401
17 Mi TY, Khanh ND, Ahuja R, *et al.* Diverse structural and electronic properties of pentagonal SiC_2 nanoribbons: A first-principles study. Mater Today Commun, 2021, 26: 102047
18 Ma LJ, Gao SQ, Jia JF, *et al.* Effects of charging, strain, and doping on the interaction between H_2 and nitrogen-rich penta-CN_2 sheet. Int J Hydrogen Energy, 2022, 47: 34183–34194
19 Wang R, He C, Chen W, *et al.* Rich B active centers in penta-B_2C as high-performance photocatalyst for nitrogen reduction. Chin Chem Lett, 2021, 32: 3821–3824
20 Liu L, Zhuang HL. PtP_2: An example of exploring the hidden Cairo tessellation in the pyrite structure for discovering novel two-dimen-

sional materials. Phys Rev Mater, 2018, 2: 114003
21 VahidMohammadi A, Rosen J, Gogotsi Y. The world of two-dimensional carbides and nitrides (MXenes). Science, 2021, 372: eabf1581
22 Ye Y, Yi W, Liu W, *et al.* Remarkable surface-enhanced Raman scattering of highly crystalline monolayer Ti_3C_2 nanosheets. Sci China Mater, 2020, 63: 794–805
23 Baghdadi A, Finley A, Russo P, *et al.* Crystal growth and characterization of PtP_2. J Less Common Met, 1974, 34: 31–38
24 Breckenridge MH, Tweedie J, Reddy P, *et al.* High Mg activation in implanted GaN by high temperature and ultrahigh pressure annealing. Appl Phys Lett, 2021, 118: 022101
25 Liu H, Xue Y, Shi JA, *et al.* Observation of the Kondo effect in multilayer single-crystalline VTe_2 nanoplates. Nano Lett, 2019, 19: 8572–8580
26 Lu HZ, Shen SQ. Quantum transport in topological semimetals under magnetic fields. Front Phys, 2017, 12: 127201
27 Shi G, Zhang M, Yan D, *et al.* Anomalous Hall effect in layered ferrimagnet $MnSb_2Te_4$. Chin Phys Lett, 2020, 37: 047301
28 Müller B, Lutz HD. Single crystal Raman studies of pyrite-type RuS_2, $RuSe_2$, OsS_2, $OsSe_2$, PtP_2, and $PtAs_2$. Phys Chem Miner, 1991, 17: 716–719
29 Morgenbesser M, Viernstein A, Schmid A, *et al.* Unravelling the origin of ultra-low conductivity in $SrTiO_3$ thin films: Sr vacancies and Ti on A-sites cause Fermi level pinning. Adv Funct Mater, 2022, 32: 2202226
30 Shen PC, Lin Y, Su C, *et al.* Healing of donor defect states in monolayer molybdenum disulfide using oxygen-incorporated chemical vapour deposition. Nat Electron, 2022, 5: 28–36
31 El-Zohry AM, Turedi B, Alsalloum A, *et al.* Ultrafast transient infrared spectroscopy for probing trapping states in hybrid perovskite films. Commun Chem, 2022, 5: 67

Acknowledgements This work was supported by the National Natural Science Foundation of China (61888102, 22178384, 21908245, and 22108301), the Ministry of Science and Technology of China (2018YFA0305800), the Chinese Academy of Sciences (ZDBS-SSW-WHC001 and XDB33030100), and the Science Foundation of China University of Petroleum, Beijing (ZX20220079).

Author contributions Li Y and Yang H supervised and coordinated the project. Cheng Q synthesized the crystal and performed most of measurements. Xian G and Guo H analyzed the magnetization and transport data. Huang Y and Chen H performed the femtosecond time-resolved absorption spectra. Zhou H and Wang J performed the temperature-dependent XRD analysis. Cheng Q, Yang H, Xian G, Guo H, and Li Y did data analysis and wrote the manuscript. All of the authors participated in analyzing the experimental data, plotting figures, and writing the manuscript.

Conflict of interest The authors declare that they have no conflict of interest.

Supplementary information Supporting data are available in the online version of the paper.

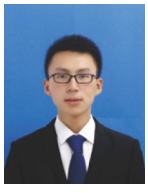

Qiuzhen Cheng is currently a PhD candidate at China University of Petroleum, Beijing. His main research focuses on the preparation and characterization of transition metal compounds and their low-dimensional materials.

Guoyu Xian is currently a PhD student at the Institute of Physics, Chinese Academy of Sciences. He received his MSc degree in physics from Hunan University in 2020. His research interest focuses on physical properties of crystals and low-dimensional materials.

Yongfeng Li is a professor at the College of New Energy and Materials, China University of Petroleum, Beijing. He obtained his PhD degree from Dalian University of Technology in 2004. He was a postdoctor at Tohoku University, Japan from 2004 to 2012. His current research interests mainly focus on the synthesis and application of new bulk and low-dimensional materials.

Haitao Yang is a professor at the Institute of Physics, Chinese Academy of Sciences. He obtained his PhD degree from the Institute of Physics in 2004. He was a postdoctor at Tohoku University, Japan from 2004 to 2008. His current research interests mainly focus on superconductivity, spin polarization, and electron correlated states of crystals and low-dimensional materials.

高质量PtP_2晶体中的三维弱局域化和负磁阻效应

程秋振[1,2†], 冼国裕[2,3†], 黄引[2,3], 郭辉[2,3,4], 潘禄禄[2], 周厚博[2,3], 王晶[2,3], 吕森浩[2], 申承民[2,3,4], 林晓[3], 陈海龙[2,3], 李永峰[1*], 杨海涛[2,3,4*], 高鸿钧[2,3,4]

摘要 近年来, 含有五元环排列结构的PtP_2单晶和二维材料因具有丰富的物理和化学性能而得到广泛关注, 有望应用于高性能电子和光电子器件. 本文通过优化Pt和P的初始摩尔比, 采用助溶剂法制备了高质量的PtP_2单晶, 并在PtP_2单晶中首次发现了三维弱局域化和负磁阻效应. 晶体结构、磁性和光谱测试表明, PtP_2单晶中的少量缺陷可抑制负磁阻效应和磁有序态. 本文提出了合成高质量贵金属磷化物单晶的有效方法, 为研究磷化物中多种关联电子态提供了新的平台.